Cosmological galaxy formation simulations using smoothed particle hydrodynamics

G. S. Stinson,[1,2★] J. Bailin,[1,3] H. Couchman,[1] J. Wadsley,[1] S. Shen,[1] S. Nickerson,[1] C. Brook[2] and T. Quinn[4]

[1]*Department of Physics and Astronomy, McMaster University, Hamilton, Ontario, L8S 4M1, Canada*
[2]*Jeremiah Horrocks Institute, University of Central Lancashire, Preston PR1 2HE*
[3]*Astronomy Department, University of Michigan, 830 Dennison Bldg., 500 Church St., Ann Arbor, MI 48109-1042, USA*
[4]*Astronomy Department, University of Washington, Box 351580, Seattle, WA 98195-1580, USA*

ABSTRACT

We present the McMaster Unbiased Galaxy Simulations (MUGS), the first nine galaxies of an unbiased selection ranging in total mass from $5 \times 10^{11} \, M_\odot$ to $2 \times 10^{12} \, M_\odot$ simulated using *N*-body smoothed particle hydrodynamics at high resolution. The simulations include a treatment of low-temperature metal cooling, UV background radiation, star formation and physically motivated stellar feedback. Mock images of the simulations show that the simulations lie within the observed range of relations such as that between colour and magnitude and that between brightness and circular velocity (Tully–Fisher). The greatest discrepancy between the simulated galaxies and observed galaxies is the high concentration of material at the centre of the galaxies as represented by the centrally peaked rotation curves and the high bulge-to-total ratios of the simulations determined both kinematically and photometrically. This central concentration represents the excess of low angular momentum material that long has plagued morphological studies of simulated galaxies and suggests that higher resolutions and a more accurate description of feedback will be required to simulate more realistic galaxies. Even with the excess central mass concentrations, the simulations suggest the important role merger history and halo spin play in the formation of discs.

Key words: methods: numerical – galaxies: evolution – galaxies: formation.

1 INTRODUCTION

Forming a galaxy like our own Milky Way remains a challenge for the currently accepted Λ cold dark matter (ΛCDM) cosmogony. The Milky Way is comprised of three distinct, stellar components: a flattened, rotating *disc*; a compact, central and spheroidal *bulge* and a diffuse, spherical *halo* of stars. Any consistent cosmogony needs to explain the origin and evolution of each of these components. ΛCDM posits that the energy budget of the Universe is currently dominated by vacuum energy (Λ), and the majority of the mass is invisible (dark) and only interacts with baryons via gravity. Thus, in the early Universe, thermal baryonic pressure did not support the dark matter, and because it is non-relativistic (cold) the dark matter first collapsed into small structures. Subsequently, the small structures merged hierarchically to form larger structures like the Milky Way.

The ΛCDM paradigm provides a simple explanation for the formation of the stellar halo: stars formed early in small satellite galax-

ies, which got tidally stripped as their orbits brought them inside the tidal radius of the main galaxy. While early observations indicated that stars in the Milky Way's halo might have condensed out of a monolithically collapsing gas cloud (Eggen, Lynden-Bell & Sandage 1962), later observations found instead that formation through mergers like those proposed in the CDM paradigm are more likely (Searle & Zinn 1978). Today, digital surveys of the sky reveal structures in the Milky Way's stellar halo such as streams and the remnant cores of dwarf galaxies (Majewski 1993; Belokurov et al. 2006). These are the exact signatures left by tidally disrupted satellites in simulations (Bullock & Johnston 2005; Abadi, Navarro & Steinmetz 2006).

Unlike haloes, discs are not so neatly explained by ΛCDM. Although conservation of angular momentum naturally creates rotating discs, the hierarchical build-up of structure impairs their formation, since discs form most efficiently in a quiet environment where gas cools and collapses smoothly. In ΛCDM-inspired simulations of substructure mergers, satellites orbiting discs tidally heat stars turning thin discs into thick discs (Toth & Ostriker 1992; Quinn, Hernquist & Fullagar 1993; Velazquez & White 1999; Kazantzidis et al. 2008). Simulations of larger galactic mergers

★E-mail: gsstinson 'at' uclan.ac.uk

transform discs into centrally concentrated, spheroidal systems as the discs experience significant angular momentum loss (Barnes & Hernquist 1996; Cox et al. 2006). However, the observed distribution of galaxy morphologies can be reproduced with simple, analytic models. In these models, uniformly rotating spheres collapse into centrifugally supported discs (Fall & Efstathiou 1980; Dalcanton, Spergel & Summers 1997; Mo, Mao & White 1998; van den Bosch 2001). The spheres start with angular momentum and mass profiles predicted using simulations of CDM structure formation. The contradiction between mergers and disc formation may indicate that halo spin, not merger history, plays the dominant role in determining the morphology of galaxies.

The bulge is a spheroid of stars at the centre of a galaxy. The spheroidal shape indicates that they formed as the result of mergers. However, other evidence reveals that some bulges may have a secular origin. Kormendy (1993) suggested that observations of rapidly rotating bulges indicates the existence of 'pseudo-bulges', and recent simulations show that the central regions of isolated discs can buckle and cause stars to evolve through 'peanut' shaped orbits into spheroidal distributions (Debattista et al. 2004).

Whether discs or spheroids form affects many galactic properties like their kinematics, colour, light distribution, star formation history (SFH) and metallicity in addition to morphology. Disc kinematics are dominated by ordered circular velocity, while in spheroidal components random velocity dominates over circular velocities. Because star formation usually happens in galaxy discs where gas densities are sufficiently high, galaxies with more prominent discs have more recent star formation and display bluer colours, while spheroids tend to be more metal-rich and red. The prominence of morphological components also has an impact on the radial distribution of galactic light profiles. Galaxies with more prominent spherical components exhibit more centrally concentrated light profiles.

Models of galaxy formation require high-resolution, hydrodynamic numerical simulations. Analytic modelling can evolve a ΛCDM-motivated Gaussian density field into a spectrum of mass structures and populate those structures with stars such that they match the observed luminosity function of galaxies (Cole et al. 2000; Benson et al. 2003; Somerville et al. 2008). However, because of the non-linear interactions of processes such as gas cooling, merging, tidal stripping, star formation, stellar feedback and active galactic nuclei (AGNs), it is difficult for these models to predict galaxy morphologies, though Benson & Devereux (2010) and Dutton (2009) represent recent attempts.

As an alternative, numerical simulations allow us to study how haloes, discs and bulges were created and evolve. Simulations that include gas are able to follow more physical processes than simulations that only track the gravitational interaction of dark matter. Gas can be modelled using smoothed particle hydrodynamics (SPH), which partitions the gas in the Universe into particles and with a Lagrangian approach follows the motions of those particles. SPH is effective because it concentrates computational resources on the high-density regions of a simulation, where galaxies form.

Several studies of galaxies in a cosmological context have generated individual objects that are similar to the observed local galaxies (Governato et al. 2004; Robertson et al. 2004; Okamoto et al. 2005; Brook et al. 2006; Governato et al. 2007; Scannapieco et al. 2008, 2009; Ceverino & Klypin 2009; Governato et al. 2009; Martínez-Serrano et al. 2009; Piontek & Steinmetz 2009; Sánchez-Blázquez et al. 2009). These require high resolution and large computational resources in order for several important properties of the simula-

tions to converge, such as the galactic structure, motions and SFH. As a consequence of the high computational cost, the initial conditions have been carefully chosen to maximize the chance that the simulation will produce the desired type of object (usually a disc galaxy).

The previous cosmological simulations have shown that the collapse of gas is more complicated than smooth collapse into centrifugally supported discs. They show that a significant fraction of gas flows into galaxies along cold filaments (Kereš et al. 2005; Brooks et al. 2009). This raises the question: are centrifugal forces all that should support discs? Observations suggest that discs derive their vertical support from an equipartition of energy between thermal, magnetic and cosmic ray pressure support (Cox 2005). It is as yet unknown how much support these forms of energy provide radially.

1.1 Stellar feedback

One way to introduce pressure support into simulations is by harnessing the energy massive stars release in stellar winds and supernovae (SNe) explosions. Recent simulations continue to suffer from the overcooling that has long plagued morphological studies of simulated galaxies. Navarro & Benz (1991) described how angular momentum transferred from gas in the disc to the dark matter causes excess central mass concentrations, which leads to massive bulges that do not compare well to observations of disc galaxies whose bulges are fainter and less massive than their discs (Allen et al. 2006). Navarro & Benz (1991) instead proposed that stellar feedback could eliminate a significant amount of low angular momentum gas. They implemented a method to kinematically excite gas particles around recently formed stars, but this showed little improvement in eliminating low angular momentum gas (Navarro & Steinmetz 2000).

Due to insufficient resolution, there is still no satisfactory treatment for stellar feedback. Multiphase gas particles attempt to capture the phenomenology of the interstellar medium (ISM) inside individual particles (Springel & Hernquist 2003a), but it is difficult to determine the appropriate pressure for each particle to exert on the others and sometimes a stiff equation of state needs to be enforced (Springel & Hernquist 2005). If the gas dynamics are separated into hot and cold gas (Pearce et al. 1999), it is ambiguous when and how much gas should move from one phase to the other. Disabling the cooling of gas heated by stellar winds and SNe causes an effective stellar feedback (Gerritsen 1997; Thacker & Couchman 2000; Stinson et al. 2006), but resolution is often insufficient to turn off cooling in the proper amount of gas for the right length of time, and SPH does not allow single particles to create their own outflow. Kinetic forms of feedback produce galactic outflows, with which simulations reproduce some of the key observed properties of galaxies (Navarro & Steinmetz 2000; Springel & Hernquist 2003b; Oppenheimer & Davé 2006; Okamoto & Frenk 2009). Whether winds should be hydrodynamically decoupled from the ISM and the appropriate parametrization of the wind velocity and the wind mass-loading to reproduce the observed satellite luminosity function and pressurize the disc remain open questions. Detailed discussions can be found in Schaye et al. (2010) and Okamoto & Frenk (2009). Many potential avenues need to be followed to see how each feedback recipe affects galaxy formation differently.

Computational resources can now support surveys that include a range of galaxies simulated at moderate (1 million dark matter particles inside r_{vir}) resolution (Okamoto & Frenk 2009; Piontek & Steinmetz 2009; Scannapieco et al. 2009) with different stellar

feedback recipes. Each survey uses SPH, and each of the previous surveys has used GADGET. Scannapieco et al. (2009) separated hot and cold gas and used supernova (SN) feedback as a conduit from the cold to the hot phase. Okamoto & Frenk (2009) used multiphase particles from Springel & Hernquist (2005) combined with driven winds of different strengths and also explore higher resolution with 10 million particles inside $r_{\rm vir}$. Scannapieco et al. (2009) found lower disc fractions than late type spirals in their simulations. Piontek & Steinmetz (2009) tested several stellar feedback recipes and did not find striking success with any of them.

In contrast to these simulated samples, observational samples of galaxies from galaxy redshift surveys, like the 2dFGRS (Colless et al. 2001) and Sloan Digital Sky Survey (SDSS; York et al. 2000), now contain millions of objects, allowing a much more complete view of not only the properties of typical galaxies, but also a quantification of how galaxies are distributed within the multivariate parameter space of galaxy properties. Evaluating the success of simulations requires a larger sample of simulated galaxies. When only a small number of simulations exist, it is easy to find a good observational match for any one simulation; however, when a *sample* of simulated galaxies exist that predict a mean and spread for any galactic property, these predictions can be directly confronted with the large observational samples.

In order to address these problems, we have begun the McMaster Unbiased Galaxy Simulations (MUGS) project. The goal of MUGS is to generate a large sample of sophisticated galaxy formation simulations that sample potential sites of L* galaxy formation in an unbiased manner for direct comparison to the large observational samples now available. In this paper, we describe the methodology used for MUGS and present an overview of the first nine simulations, particularly focusing on the relative formation of discs and bulges.

MUGS provides an extended look at galaxies simulated using similar physics to Governato et al. (2007) and Governato et al. (2009). Namely, SNe are modelled with adiabatic 'blastwave' feedback described in Stinson et al. (2006). In Section 2, we describe how we created the initial conditions for MUGS. Section 3 details the algorithm that evolves the simulations. Section 4 examines the properties of the galaxies including their brightness, colour, mass-to-light ratios, density profiles, bulge-to-total ratio, SFH and metallicity.

2 SIMULATIONS

The simulations that comprise the MUGS sample each use the volume renormalization techniques used in many previous simulations. The technique allows high resolution in a cosmological context at reasonable computational cost. It focuses resolution in one specific region of a cosmological volume while simulating the rest of the volume at lower resolution. The surrounding volume provides large-scale density waves that impart tidal torques on the region of interest (Quinn & Binney 1992).

We selected our galaxies from a cosmological cube $50\,h^{-1}$ Mpc on a side containing 256^3 dark matter particles that was evolved to $z = 0$. The simulation is based on a 4096^3 realization of the CMBFAST (Seljak & Zaldarriaga 1996) power spectrum initially subsampled to 256^3 to create a uniform resolution, dark-matter-only volume. It uses a *Wilkinson Microwave Anisotropy Probe Three* (*WMAP*3) ΛCDM cosmology with $H_0 = 73$ km s^{-1} Mpc^{-1}, $\Omega_{\rm m} = 0.24$, $\Omega_\Lambda = 0.76$, $\Omega_{\rm bary} = 0.04$ and $\sigma_8 = 0.76$ (Spergel et al. 2007).

The uniform volume was evolved to $z = 0$ at which point the friends-of-friends algorithm was used to find the virialized haloes

with a linking length $= (1/5)$ interparticle separation (Davis et al. 1985). Every group with a mass between 5×10^{11} M$_\odot$ (705 particles in 256^3) and 2×10^{12} M$_\odot$ (2820 particles in 256^3) was examined to ensure that it did not evolve closer than 2.7 Mpc from any halo more massive than 5×10^{11} M$_\odot$. Massive structures contain hot gas that would significantly alter the evolution of a galaxy of interest. Simulating structures larger than 2×10^{12} M$_\odot$ to $z = 0$ at the resolution of these galaxies is currently computationally unfeasible. Out of the 36 193 haloes found with friends-of-friends, 761 were in the right mass range and 276 of those were sufficiently isolated. From that sample, nine haloes were randomly selected for more detailed simulation without regard for spin parameter or merger history.

Individual initial conditions were specified for each galaxy as follows. Particles within $5r_{\rm vir}$ of each groups centre at $z = 0$ were traced to their positions in the initial conditions; this specifies the 'region of interest' for each simulation. In an effort to efficiently use computational resources without loss of physical veracity, the region of interest is not expanded to be a sphere but is allowed to have a non-spherical shape. (Minimizing the number of particles is critical for maintaining a computationally tractable problem.) The region of interest was then filled with particles occupying the points from a regular lattice that lay within this region. An effective resolution of 2048^3 was achieved at the centre. Surrounding the non-spherical region of interest is a spherical region with a radius 1.2 times the maximum radius of the region of interest. This immediately surrounding region is populated with particles leading to an effective resolution of 512^3. Outside this are three further spherical regions equally spread in radius with effective resolutions of 256^3, 128^3 and 64^3. The remaining outskirts of the $50\,h^{-1}$ Mpc cube are filled at an effective resolution of 32^3. Each of these regions contains progressively more massive particles corresponding to the reduced resolution. Using this scheme, there are between four and 10 times more particles in the high-resolution region of interest than in the surrounding low-resolution regions combined. The regular grids of particles in each region were perturbed using the Zel'dovich approximation with subsampled force resolutions matching the particle resolutions.

This dark matter-only configuration was evolved to $z = 0$. The particles that ended up inside $3r_{\rm vir}$ in the dark matter-only resimulation had a fraction of their mass converted into a separate, neighbouring gas particle with a mass corresponding to the cosmic baryon fraction, $\Omega_{\rm b}/\Omega_{\rm m}$. We then reapplied the Zel'dovich perturbations to this new regular grid. Fig. 1 shows the initial configuration for a sample galaxy. In the high-resolution region, dark matter particles have a mass of 1.1×10^6 M$_\odot$ and gas particles have an initial mass of 2.2×10^5 M$_\odot$. All stars form with a mass of 6.3×10^4 M$_\odot$. Each particle uses a gravitational softening length of 312.5 pc.

2.1 Galaxy sample

One of the main goals of this study is to develop a better understanding of what sorts of galaxy morphologies are created using a wide range of initial conditions. The randomly selected MUGS sample spans a wide range of merger histories and halo angular momenta. The merger history is characterized as the redshift at which the galaxy obtained half of its final mass. The angular momentum of each halo is characterized by $\lambda' = J/\sqrt{5/3GM^3R}$ (Bullock et al. 2001). Fig. 2 shows how the λ' and half mass redshifts of the haloes in our nine halo sample compare to the distribution of haloes that passed our selection criteria. The λ' values shown in Fig. 2 are the
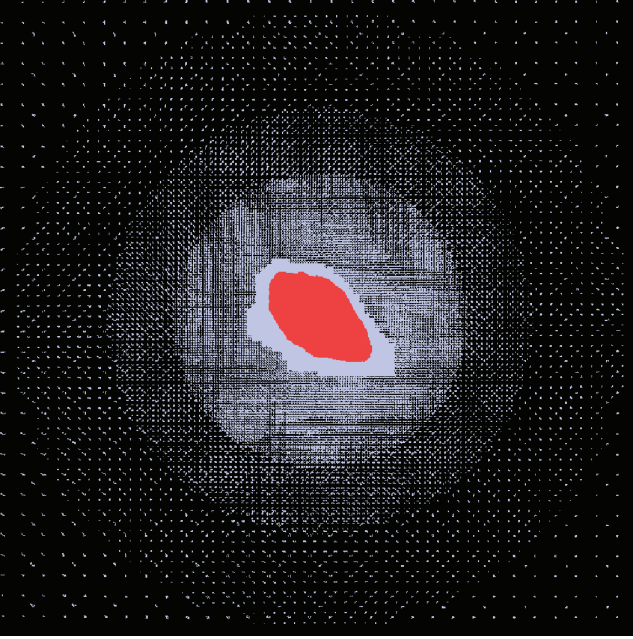
Figure 1. Projection of initial particle configuration for g15784. The red particles represent gas and the light blue represents dark matter. Gas is only included in the high-resolution region at the centre. The dots become less dense further away from the centre because of the decreased resolution and higher particle masses at larger radii.

values from the low resolution, uniform dark matter-only simulation. The values found when the galaxies are run at high resolution including baryonic physics vary modestly from these values. Fig. 2 shows that in the initial sample of nine galaxies does not include any from the high λ' tail. As the sample grows in the future, it will more fully reproduce the multivariate distribution of halo properties. We note that only one halo with half mass redshift greater than 1.5 has a λ' values greater than 0.05, but that some of the haloes that accrete half of their mass later have λ' values that surpass 0.1. Ryden (1988) point out that late accretion contributes more angular momentum to haloes because of their larger turnaround radius. It is expected that galaxies with the quietest merger histories will form galaxies with the most prominent discs.
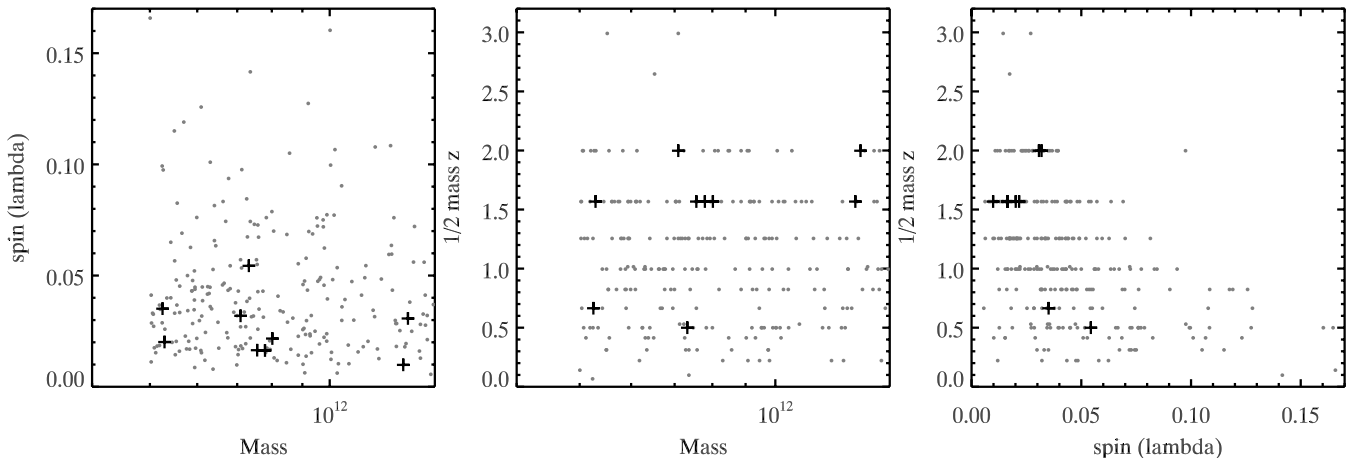
3 CODE

The simulations were evolved using the parallel SPH code GASOLINE (Wadsley, Stadel & Quinn 2004). GASOLINE solves the equations of hydrodynamics, and includes radiative cooling. Gravity is calculated for each particle using a tree algorithm similar to Barnes & Hut (1986) but using a K-D tree with tree elements that span at most $\theta = 0.7$ of the size of the tree element's distance from the particle. GASOLINE is multistepping so that each particle calculates its forces once every gravitational time-step $\Delta t_{\text{grav}} = \eta\sqrt{\epsilon_i/a_i}$, where $\eta = 0.175, \epsilon_i$ is the gravitational softening length (312.5 pc) and a_i is the acceleration. For gas particles, the time-step must also be less than $\Delta t_{\text{gas}} = \eta_{\text{Courant}}(h_i/c_i)$, where $\eta_{\text{Courant}} = 0.4, h_i$ is the gas smoothing length and c_i is the sound speed.

The cooling is calculated from the contributions of both primordial gas and metals as $\Lambda_{\text{tot}}(z, \rho, T, Z) = \Lambda_{\text{HI,HeI,HeII}}(z, \rho, T) + (Z/Z_{\odot})\Lambda_{\text{metal},z_{\odot}}(z, \rho, T)$. The primordial cooling follows the non-equilibrium evolution of internal energy along with three primordial gas species (H I, He I and He II). H$_2$ cooling is not included. The scheme uses the collisional ionization rates reported in Abel et al. (1997), the radiative recombination rates from Black (1981) and Verner & Ferland (1996) and bremsstrahlung and line cooling from Cen (1992). The metal cooling grid is constructed using CLOUDY (version 07.02, last described by Ferland et al. 1998), assuming ionization equilibrium. A uniform ultraviolet ionizing background, adopted from Haardt & Madau (in preparation; see also Haardt & Madau 1996), is used in order to calculate the metal cooling rates self-consistently. The cooling lookup table is linearly interpolated in three dimensions (i.e. ρ, z, T) and scaled linearly with metallicity. The energy integration independently uses a semi-implicit stiff integrator for each particle with the compressive heating and density (i.e. terms dependent on other particles) assumed to be constant over the time-step.

The star formation and feedback recipes are the 'blastwave model' described in detail in Stinson et al. (2006) with additional improvements as described in Section 3.1. They are summarized as follows. Gas particles must be dense ($n_{\text{min}} = 0.1 \, \text{cm}^{-3}$) and cool ($T_{\text{max}} = 15\,000$ K) to form stars. A subset of the particles that pass these criteria are randomly selected to form stars based on the commonly used star formation equation,

$$\frac{\mathrm{d}M_{\star}}{\mathrm{d}t} = c^{\star}\frac{M_{\text{gas}}}{t_{\text{dyn}}}, \tag{1}$$

Figure 2. Three projections of the galaxy sample in mass, spin and half mass redshift space. The light dots represent all the galaxies in our sample mass range from the uniform volume. The plus signs indicate the galaxies presented here.

where $M_\star$ is mass of stars created, $c^\star$ is a constant star formation efficiency factor, M_{gas} is the mass of gas creating the star, dt is how often star formation is calculated (1 Myr in all of the simulations described in this paper) and t_{dyn} is the gas dynamical time. The constant parameter, $c^\star$, is tuned to 0.05 so that the simulated isolated model Milky Way used in Stinson et al. (2006) matches the Kennicutt (1998) Schmidt Law, and then $c^\star$ is left fixed for all subsequent applications of the code. This star formation and feedback treatment was one of the keys to the success of Governato et al. (2007) in producing realistic spiral galaxies in a cosmological simulation and the success of Brooks et al. (2007) in matching the observed mass–metallicity relationship.

At the resolution of these simulations, each star particle represents a large group of stars (6.32×10^4 M$_\odot$). Thus, each particle has its stars partitioned into mass bins based on the initial mass function (IMF) presented in Kroupa, Tout & Gilmore (1993). These masses are correlated to stellar lifetimes as described in Raiteri, Villata & Navarro (1996). Stars larger than 8 M$_\odot$ explode as SNe during the time-step that overlaps their stellar lifetime after their birth time. The explosion of these stars is treated using the analytic model for blastwaves presented in McKee & Ostriker (1977) as described in detail in Stinson et al. (2006). While the blast radius is calculated using the full energy output of the SN, less than half of that energy is transferred to the surrounding ISM, $E_{SN} = 4 \times 10^{50}$ erg. The rest of the SN energy is assumed to be radiated away. Iron and oxygen are produced in Type II SNe (SNeII) according to the analytic fits used in Raiteri et al. (1996):

$$M_{Fe} = 2.802 \times 10^{-4} M_\star^{1.864} \tag{2}$$

$$M_O = 4.586 \times 10^{-4} M_\star^{2.721}. \tag{3}$$

The iron, oxygen and the SN energy ejected from SNII are distributed to the same gas within the blast radius. Each Type Ia SNe (SNeIa) produces 0.63 M$_\odot$ iron and 0.13 M$_\odot$ oxygen (Thielemann, Nomoto & Yokoi 1986) and ejects it into the nearest gas particle for SNIa.

3.1 Quantized stellar feedback

One of the aspects of stellar feedback not given detailed consideration in Stinson et al. (2006) is the clustered nature of star formation. In Stinson et al. (2006), SN feedback is chronologically distributed according to the stellar IMF and lifetimes. The combination of Padua group stellar lifetimes with the Kroupa et al. (1993) IMF results in a constant, small energy release each feedback time-step (1 Myr, concurrent with star formation) for the 35 Myr until the lowest mass stars that explode as SNe (8 M$_\odot$) explode. Since the blastwave radius and cooling shut-off time are calculated from the energy released during a time-step, the Stinson et al. (2006) method results in small blastwaves. McCray & Kafatos (1987) describe how the accumulated energy of stellar winds and SN feedback create large superbubbles around star clusters. With a stochastic treatment of the energy release timing, we use the accumulated energy of all the stellar feedback that should result from a star particle to produce a larger, more realistic blastwave. The larger blastwaves should provide more pressure support to make more extended discs. Using a Kroupa et al. (1993) IMF, one SN mass (>8 M$_\odot$) star is created for every 200 M$_\odot$ of stars that form. Combining globular cluster (Harris 1996), open cluster (Piskunov et al. 2008) and embedded cluster (Lada & Lada 2003) catalogues, we estimate that a typical star forms in a cluster of 4000 M$_\odot$. Thus, we require a

minimum energy release of 20 SNe (2×10^{52} erg) for the MUGS simulations.

We stochastically determine when a star particle releases feedback energy,

$$p = \frac{N_{SNII} \bmod N_{SNQ}}{N_{SNQ}} \tag{4}$$

$$N_{ESN} = \text{floor}\left(\frac{N_{SNII}}{N_{SNQ}}\right) + \begin{cases} 0, & r \le p \\ N_{SNQ}, & r > p \end{cases} \tag{5}$$

where N_{SNII} is the number of SNe calculated to explode during that star formation time-step, N_{SNQ} is the 'SN quantum', the number of SN required per explosion and N_{ESN} is the total number of SN explosions that will have their energy distributed during a the star formation time-step. If the probability, p, is greater than a random number, r, selected between 0 and 1, N_{SNQ} SNe's worth of energy is released. This causes SN energy to be released sporadically over the 35 Myr until the largest star remaining is <8 M$_\odot$.

4 RESULTS

In this section, we examine the galaxies that form from our set of cosmological initial conditions. First, we compare the properties of mock images of the simulated galaxies with observed galaxies. Secondly, we examine which parameters have the greatest impact on how much disc or spheroid forms. Thirdly, we compare how much light is produced in our galaxies with observations of the Tully–Fisher relationship and weak lensing mass measurements. Finally, we present the SFHs) and metallicity trends for the simulated galaxies.

4.1 Tabulated results

In order to identify the main halo and its satellites, we used the AMIGA Halo Finder (AHF) (Knollmann & Knebe 2009). AHF overcomes the difficulties friends-of-friends has in separating neighbouring groups, by instead identifying density peaks using an adaptive mesh algorithm. The adaptive mesh algorithm naturally leads to identification of substructure, which is critical for analysing cosmological simulations. Table 1 summarizes key properties for each of the galaxies found with AHF in the sample. Galaxies are identified using the group number from the original friends-of-friends galaxy catalogue. The columns are described below.

The columns are defined as follows. Mass is the total mass in 10^{11} M$_\odot$ located inside r_{vir} at $z = 0$ of the final simulation including baryonic physics. λ' is the spin parameter of that matter defined as $\lambda' = (J/\sqrt{5/3GM^3 r_{vir}})z_{lmm}$ is the redshift of the last major merger, which is defined as the redshift when the AHF no longer distinguished a satellite from the main halo where the satellite stellar mass was greater than one-third the stellar mass of the main halo at any point in its history. $z_{1/2}$ is the redshift when the main halo was one-half its mass at $z = 0$. M_{gas} is the mass of gas inside r_{vir} at $z = 0$. f_b is the baryon fraction of the final halo ($M_{star} + M_{gas}/M_{tot}$). M_* is the mass of stars inside r_{vir} at $z = 0$. M_{disc} and M_{SPH} are the mass of stars kinematically classified as part of the disc and spheroid, respectively, as described in Section 4.4. All the gas and stellar masses are reported in 10^{10} M$_\odot$. The numbers of gas, star and dark matter particles inside r_{vir} at $z = 0$ are N_{gas}, N_* and N_{DM}, respectively.

One of the problems inherent in running simulations where only a localized region is populated with high-resolution particles is that it is possible for low-resolution particles or particles from outside

Table 1. Simulation data.

Galaxy	Mass (10¹¹ M⊙)	λ'	z_{lmm}	$z_{1/2}$	f_b	M_{gas} (all	M_* masses	M_{disc} in	M_{SPH} 10¹⁰ M⊙)	N_{gas} 10⁵	N_* 10⁶	N_{DM} 10⁵	Gasless DM
g1536	7.0	0.025	2.9	1.8	0.159	5.1	6.0	1.8	3.9	2.4	1.4	5.3	1640
g5664	5.2	0.025	3.4	1.3	0.164	3.8	4.8	1.3	3.3	1.8	1.1	4.0	0
g7124	4.5	0.039	2.0	1.5	0.163	2.5	4.8	0.12	3.2	1.1	1.1	3.4	147
g15784	14	0.0345	2.5	1.4	0.150	10	11	3.3	5.5	4.8	2.6	11	2
g21647	7.7	0.048	0.03	0.53	0.168	5.8	7.1	1.1	3.3	2.7	1.6	5.8	6
g22437	8.8	0.013	1.6	1.2	0.170	7.6	7.3	0.56	5.6	3.5	1.6	6.6	1
g22795	8.7	0.011	4.0	1.3	0.144	6.0	6.4	0.26	5.4	2.7	1.5	6.6	76
g24334	7.7	0.041	1.3	1.2	0.162	7.1	11	1.1	5.4	3.3	2.4	8.2	60
g25271	13	0.014	2.2	1.3	0.147	8.9	11	2.2	7.2	4.0	2.4	10	3

the gas region to pollute the region of interest and cause unphysical results. No low-resolution particles lie within r_{vir} at $z = 0$ of any of the MUGS simulations. Some dark matter particles (gasless DM) that originated outside the gas region ended up inside the virial radius. The presence of these particles without corresponding gas indicates that some of the gas in the simulation experienced slightly less pressure than in reality. The initial conditions for g1536 were the first ones that were generated, before the final criteria were firmly in place, and only contained gas particle pairs for dark matter particles that ended up inside r_{vir}; as a consequence, it contains many more bad DM particles than the other simulations.

4.2 Simulated images

The most intuitive way to compare simulations with observations is through mock images of the simulations. Such images can be created by assigning stellar population models like Starburst99 (Leitherer et al. 1999) to each star particle to determine the colour and luminosity each star particle should contribute to an image. Additionally, dust can modulate the image with extinction and scattering. SUNRISE (Jonsson 2006) is a Monte Carlo ray tracing program that produces simulated images by assuming dust exists in metal rich gas. Fig. 3 shows images 50 kpc on a side that include scattering and absorption and are produced using SUNRISE. The image brightness and contrast are scaled using *asinh* as described in Lupton et al. (2004) since discs have an exponential surface brightness profiles meaning the images span a wide range in surface brightness.[1]

Each galaxy is aligned so that the total angular momentum of the gas inside 1 kpc is pointed upwards in Fig. 3. This presents the simulated galaxies edge-on to demonstrate the relative size of the disc and spherical component. In several of the images, a thin disc of young, blue stars is surrounded by a halo of old, red stars. In other images, little disc component is evident and the spherical component dominates. We note that several of the galaxies (g5664, for example) are not perfectly aligned indicating that the discs are warped or that the stars are orbiting around a slightly different axis than the gas. Gas is used for alignment rather than stars because gas defines the most current central disc. 1 kpc was chosen as the radius because all the galaxies including the gas poor red galaxies contained some gas disc in this innermost region. g7124 appears to be elongated vertically rather than horizontally because it is dominated by its spheroid which is strongly elongated perpendicular to its angular

momentum of the inner gas, i.e. it is a spheroid rotating about the minor axis.

In contrast to the images presented in Fig. 3, the magnitudes and surface brightnesses used throughout the rest of the paper are derived from the face-on projection of the galaxies generated by SUNRISE, for which the extinction effects are minimized.

4.3 Colour–magnitude relationship

One simple quantitative evaluation of the simulations is how the colour and brightness of galaxies compare to observations. Fig. 4 shows a $g - r$ versus absolute r colour–magnitude diagram (CMD) of $\sim 3 \times 10^5$ galaxies from the SDSS as the shaded two-dimensional histogram (Bailin & Harris 2008). The colours and magnitudes have been inclination-corrected to their expected face-on values. The two well-known features of the observed CMD are the relatively narrow red sequence, which extends to very bright galaxies, and the more broad blue cloud, which is abruptly truncated at $M_r \sim -23$. Relatively few galaxies are observed to lie in the intermediate 'green valley'. The simulated galaxies are overplotted as the labelled points.

The first conclusion that can be drawn from Fig. 4 is that the simulated galaxies lie in observationally populated regions of the CMD; they are representative of the colours and magnitudes of observed galaxies. Three simulated galaxies, g7124, g22795 and g25271, lie on the red sequence while the remainder are members of the blue cloud. This is a slightly smaller proportion than the 48 per cent of SDSS galaxies that lie on the red sequence [within 0.08 of the mode of the red sequence, i.e. the Bailin & Harris (2008) CMD parameter, $CMD^F > -0.08$]. Given the small size of the simulated sample, this difference should not be overinterpreted. However, a physical reason to expect different red sequence fractions is that the two samples are found in different environments: many observed galaxies are cluster members lying in massive haloes, while the simulated galaxies all lie at the centres of galaxy-mass haloes.

This is demonstrated in Fig. 5, where we have used the group catalogue of Yang et al. (2007) to restrict the observational sample to central galaxies of haloes with masses $4 \times 10^{11} \, M_\odot \leq M_{halo} \leq 2 \times 10^{12} \, M_\odot$, and that do not have a neighbouring group with halo mass $> 3 \times 10^{12} \, M_\odot$ within 500 km s⁻¹ and a projected radius of 2 Mpc. This is essentially identical to the selection criteria for our simulated galaxies. The relative fractions of blue versus red galaxies in Fig. 5 are indistinguishable from those of our simulated sample: 30 per cent for the observed sample and $3/9 = 33$ per cent for the simulated sample. It is also apparent from this figure that not only do the simulated galaxies lie within the observed ranges of colour

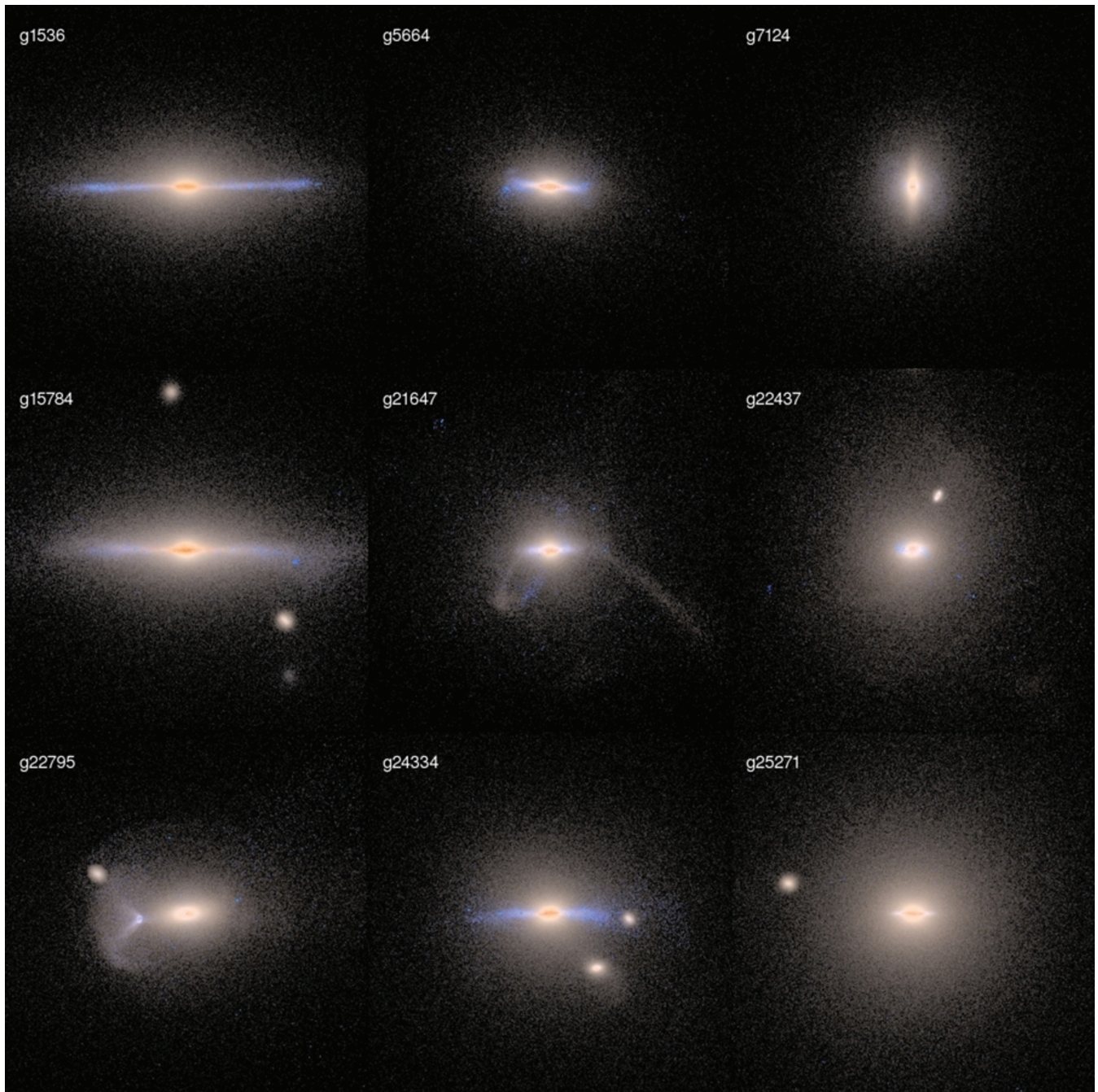[1] Face-on images and movies of the galaxies forming can be found at http://mugs.mcmaster.ca.

Figure 3. Edge-on mock images of the simulated galaxies using the *g*, *r* and *i* filters found using the Monte Carlo radiative transfer program SUNRISE. Each image is a two-dimensional projection of a box 50 kpc on a side.

and magnitude for the global SDSS population, but they are also a particularly good match to observed galaxies that lie in haloes of the correct mass and environment (although perhaps somewhat too luminous, a point we will return to in Section 4.7).

While the MUGS galaxies are representative of some observed galaxies, they are unusually 'green': the red sequence galaxies lie on the blue edge of the sequence, while the blue cloud galaxies lie in the red half of the cloud. The simulated red sequence galaxies therefore have more star formation activity than usually observed, while the blue cloud galaxies have either less recent or more ancient star formation than observed galaxies. One explanation for the sustained star formation in the red sequence galaxies is that it is a

consequence of the environmental effects noted above. However, the simulated galaxies are also too blue in Fig. 5, which takes these environmental effects into account. Their blue colour could also highlight some numerical failure of our simulations. MUGS does not include AGN feedback, which might be able to drive significantly more star-forming gas out of the central regions of galaxies. The blue colour may also result from overcooling, where lack of resolution causes excess gas to be driven to the galaxy centre where it cools rapidly and forms stars due to the high gas density. When the stars formed in the last 5 Gyr of the simulation are excluded from the SUNRISE image, their colours redden by 0.1 dex, moving them to the red side of the red sequence. Thus, quenching star
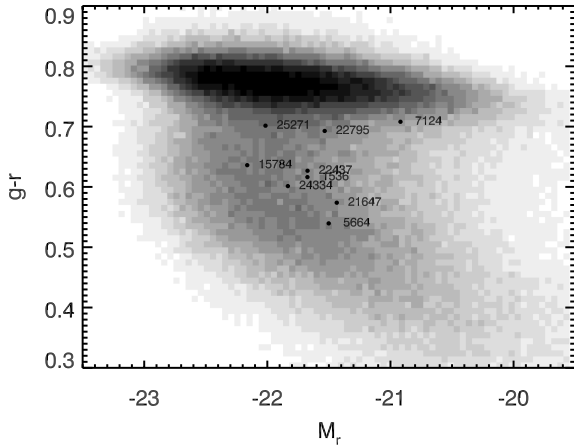
Figure 4. Simulated galaxy $g - r$ colour as a function of absolute r magnitude in the SDSS filter bandpasses overlaid on an inclination corrected CMD of SDSS galaxies from $z < 0.2$ from Bailin & Harris (2008).
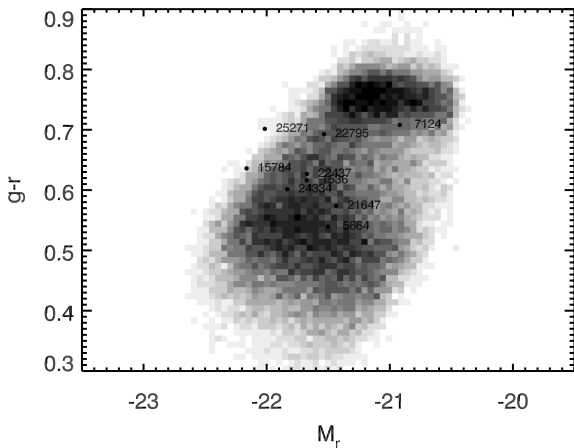

Figure 5. As in Fig. 4, but with the SDSS sample restricted to isolated central galaxies with the same halo mass range as the simulated sample.

formation sooner would produce galaxies that better match the red sequence.

The redness of the simulated blue cloud galaxies could also be a natural result expected for moderate mass galaxies evolving in an isolated environment, though Fig. 5 again suggests that this is not the case. Alternatively, it could be the result of excess ancient star formation due to our neglect of the increased feedback from metal-free Population III stars, or overcooling of gas that resulted in too many stars formed in the dense centres of galaxies at early times. Overcooling can in fact simultaneously make the blue galaxies too red by building too large of a bulge (as seen in Section 4.4), and make the red galaxies too blue by continuing to provide cold gas to the centres of bulge-dominated galaxies at late times.

Regardless of these details, the colours and magnitudes of the simulated galaxies agree well with those of observed galaxies, giving us confidence that analysing them will provide a template of how galaxies form in the real universe.

4.4 Bulge versus disc

Another quantitative comparison between simulated galaxies and observations is how the light and matter are distributed. Fig. 6 shows the face-on i-band surface brightness profiles of the simu-
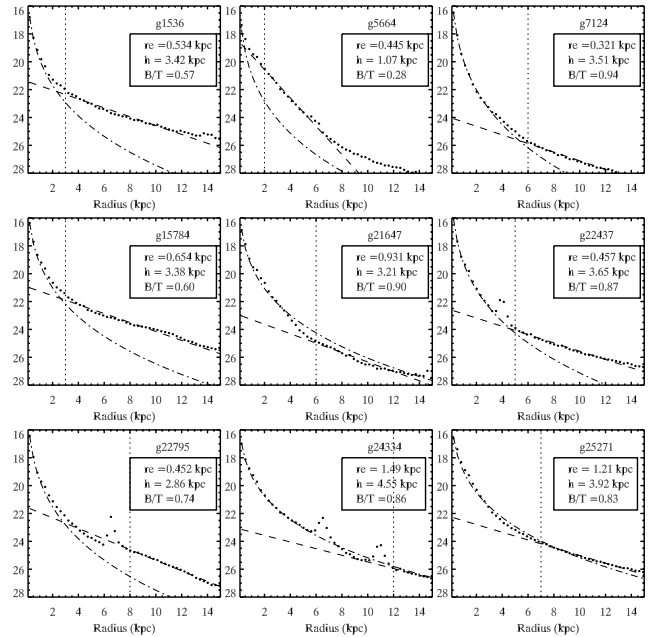

Figure 6. Surface brightness profiles of face-on mock i-band images of the simulated galaxies, created using SUNRISE. The profiles are fit with the sum of an $r^{1/4}$ law and an outer exponential disc. The bulge-to-total ratios are calculated using equation (6).

lated galaxies each fit with the sum of a de Vaucouleurs $r^{1/4}$ law (with effective radius, r_e) and exponential disc (with scalelengths, h) profiles. We calculate a ratio of the light from the bulge to the total light of the galaxy using

$$B/T = \frac{I_e r_e^2}{I_e r_e^2 + I_d h^2} \tag{6}$$

(Binney & Merrifield 1998). All the B/T ratios shown in Fig. 6 except g5664 are higher than 0.5, indicating that bulges dominate the emission from nearly all of our galaxies. In contrast, observed B/T ratios for galaxies with classical bulge/disc profiles are often <0.5, [see, e.g. fig. 8 of Allen et al. (2006) base on the observed Millennium Galaxy Catalog]. Again, the high B/T ratios in the simulations indicate that too many stars form in the central region.

Galaxies can also be separated into bulge and disc components based on their kinematics. For this analysis, discs are again aligned such that the angular momentum of the gas within 1 kpc of the centre of the halo points along the z-axis. Fig. 7 shows the stellar distribution of j_z/j_c as a function of its three-dimensional radius from the centre. j_z is the z-component of the specific angular momentum vector to the specific angular momentum. j_c is the specific angular momentum of an ideal circular orbit at the radius where the star is orbiting. Stars were sorted into a grid with 100 bins along each axis. The strength of the grey-scale is weighted by the square root of the stellar density in each bin. Substructures identified by AMIGA have been removed, though remnant substructures appear in g22437, g22795 and g25271.

Stars within 25 kpc of the galactic centre are classified as belonging to the disc if j_z/j_c is greater than 0.7, but less than 1.5 (dashed lines). Stars orbiting with $j_z/j_c > 1.5$ are at the pericentre of radial orbits likely heated by interactions. Though bulges can vary in size, we classify all material inside 5 kpc outside the disc j_z/j_c constraints as part of the bulge. Substructures, stars outside 5 kpc and the disc j_z/j_c constraints, and all stars outside 25 kpc are classified as part of the halo. The ratio of the masses of the bulge to the bulge plus the
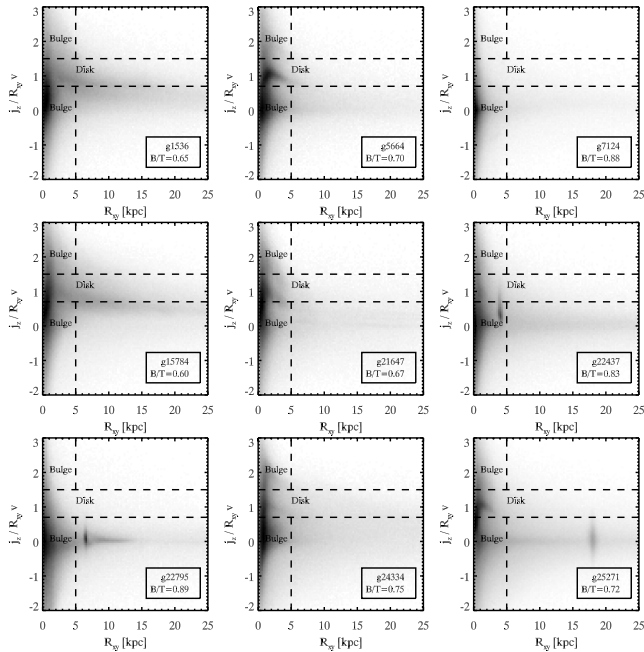
Figure 7. The ratio of the z-component of the specific angular momentum vector, j_z, to the specific circular angular momentum for a star orbiting at the same radius, $j_c(r) = v_c R_{xy}$ for every star particle. Stars are sorted into 100×100 bins 0.04 wide in $\log(r)$ and 0.02 high in j_z/j_c. The dashed lines are drawn to show how stars are classified into disc, bulge and halo components. Stars with $R_{xy} < 25$ kpc and $0.7 < (j_z/j_c) < 1.5$ are classified into the disc. Stars outside that j_z/j_c range and inside $R_{xy} < 5$ kpc are classified in the bulge. All other stars including every star AMIGA classifies as part of substructures are classified as halo stars.

disc is given as the bulge to total (B/T) ratio. Note, though this is not the same bulge-to-total ratio derived photometrically as in Fig. 6, the results are similar as the mass of stars in the bulge is most often greater than the mass in the disc. Since the 40-kpc radius is much larger than what is generally considered part of the bulge, hereafter we refer to the kinematically defined component as the spheroid.

Several features stand out in Fig. 7. The majority of the stellar mass is concentrated in the central 2 kpc of the galaxy. An exponential matter distribution will always exhibit a high central concentration, though as shown in Fig. 6, stars may be more centrally concentrated in simulations than they are in reality. In the majority of the galaxies, the values of j_z/j_c are located above 0, which shows that the bulge is rotating in many of these galaxies. There are disc features that gradually decline from $j_z/j_c = 1$ to 0.5. The decline must be due to disc heating that happens at large radius either in the form of warps or other excursions of the angular momentum from alignment with the gas disc.

4.4.1 What creates the discs?

The bulge/disc decompositions show that MUGS simulations remain crude representations of the formation of disc galaxies; the bulge fractions are much larger than what are observed. Still, young stellar discs are apparent in at least g1536 and g15784 in Fig. 3, so we briefly examine which halo properties correlate with disc formation in the simulations. Fig. 8 shows the photometric bulge-to-total ratio for the galaxies as a function of mass, final spin parameter (λ') and the redshift of the last major merger. The use of unbiased simulations allows us to draw conclusions from these plots because

no selection criteria was based on those variables. One exception to our use of the photometric B/T ratio is g5664, which is the only galaxy with significantly different photometric and kinematic B/T ratios. The photometric decomposition for g5664 is unusual, and seems to display two distinct exponential components. The total bulge+disc fit is therefore poor and the decomposition based on that fit is suspect. Thus, for g5664, we have plotted the mean of the kinematic and photometric B/T ratios in Fig. 8.

A correlation is apparent between z_{lmm} and B/T. Galaxies with the most recent last major mergers have the largest bulges. The galaxies with the reddest colours in Fig. 4, g7124, g22795 and g25271, all have significant bulges and had their last major mergers prior to $z = 2$. Both g25271 and g22795 have low-spin parameter values. The movies of these galaxies[2] show that they were involved in enough retrograde minor mergers that they never had a chance to grow a significant disc. g7124 does not have a movie, but a close examination of its outputs reveals a similar harassment filled history.

We note that the galaxies with the most significant bulge separate into two groups: one with higher spin and one with lower spin. The higher spin galaxies all experienced recent last major mergers (also see D'Onghia & Navarro 2007). This indicates that it is only possible for galactic haloes to gain angular momentum sufficient to increase its spin parameter above 0.04 if it has a late major merger. We further note that these galaxies with a high-spin parameter display the largest bulge fractions. Observed giant low surface brightness (LSB) galaxies also exhibit large bulges (Lelli, Fraternali & Sancisi 2010). This might confirm the predictions of analytic models of galaxy formation (e.g. Dalcanton et al. 1997) that haloes with the highest spin parameters should host LSB galaxies. Governato et al. (2009) showed how discs can form after late major mergers, but refrained from making any direct comparisons to LSB galaxies.

The lower spin group experienced a wide range of merger histories. Based on their spin parameters, it is apparent that the haloes containing the galaxies did not contain sufficient angular momentum to form discs.

4.4.2 What creates the spheroids?

Every galaxy in our sample displays a dominant spheroidal stellar component in both photometric and kinematic decompositions. Since spheroids easily form as the result of merging, we examine the formation of the spheroid in the simulation that has the quietest merger history and largest disc (g15784) here to discover whether there are any significant secondary effects. We leave study of spheroid formation in the other galaxies for future work.

Fig. 9 shows the formation history of the stars in the spheroid at $z = 0$. The spheroid stars are separated into three categories based on where they formed: (1) in satellites; (2) within 1 kpc of the centre of the main galaxy or (3) in the disc of the main galaxy. We emphasize that stars in the disc category are no longer part of the disc, but are spheroid stars that formed in the disc. The decomposition was based on the distance stars formed from the centre of the main halo. The stars were sorted into bins 1 Myr in length based on their formation time. The centre of mass of the stars that formed during that time was calculated by combining the stars formation locations in each time bin with the centre of the main halo found using the AHF (Knollmann & Knebe 2009) at the nearest output (generally full outputs were only written every 100 Myr). The large number of stars that formed within the central kpc of the main halo made

---
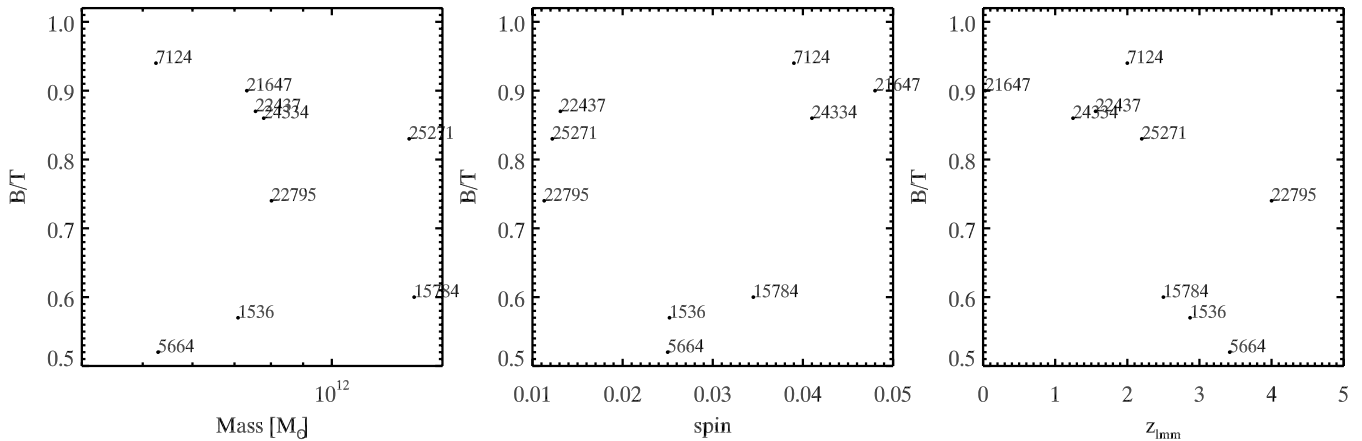
[2] found at http://mugs.mcmaster.ca

Figure 8. The photometric bulge-to-total ratios shown in Fig. 6 as a function of galaxy mass, spin and last major merger redshift. Galaxies at the bottom of these plots exhibit the strongest discs although they still have $B/T > 0.5$.
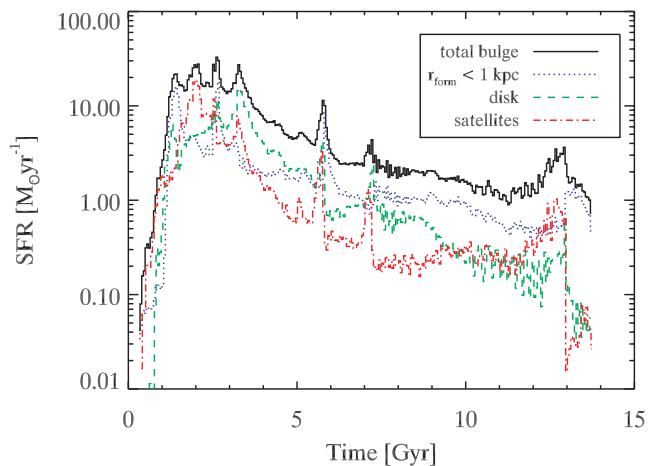

Figure 9. Formation history of stars kinematically classified as part of the spheroid in g15784 at $z = 0$. The solid line shows the total SFH for all the stars that comprise the spheroid at $z = 0$. The blue dotted line shows the portion of that total that formed in the central 1 kpc of the main halo. The green dashed line shows the portion that formed in the disc and was heated to the spheroid. The red dot–dashed line shows the portion of the inner 40-kpc spheroid that formed in satellites.

finding the star formation centre straightforward for the MUGS galaxies. We calculated the three-dimensional distance between the centre and the stars that formed during each time interval, and placed them into radial bins 1-kpc wide. Because the stellar density drops strongly at the edge of the disc, the existence of an empty radial bin serves as a delineation between the main galaxy and satellites. We therefore classify all stars within this radius (but outside of 1 kpc) as 'disc-formed' stars, and all stars outside of this radius as 'satellite-formed' stars. The total bulge stellar mass is $7.7 \times 10^{10}\,\mathrm{M_\odot}$, the mass formed inside 1 kpc is $2.6 \times 10^{10}\,\mathrm{M_\odot}$, the mass formed in the disc is $2.6 \times 10^{10}\,\mathrm{M_\odot}$ and the mass formed in satellites is $2.2 \times 10^{10}\,\mathrm{M_\odot}$.

The final merger that disturbs stars from the disc into the spheroid happens about 13 Gyr into the simulation. After that time, nearly all the stars that constitute the spheroid form in the central 1 kpc. These are the stars that have $j_c/j_z > 0$, indicating their net rotation in Fig. 7. Stars forming in the poorly resolved central kpc is not limited to the final Gyr, they are a constant source of spheroid stars throughout the evolution of g15784. For a significant fraction of the

history of g15784, the mass of stars formed in the central kpc of the main halo is similar to the mass of stars formed in satellites. While the formation of stars in the central 1 kpc is reminiscent of observations of rapidly rotating pseudo-bulges (Kormendy 1993), we cannot draw any firm conclusions since the inner 1 kpc is poorly resolved in these simulations.

Stars that form in the disc also contribute a large fraction of stars to the final spheroid, though a merger 6 Gyr into the simulation marks the end of the dominant contribution of disc stars to the spheroid. We leave a detailed examination of how stars migrate from the disc to the spheroid for future work, but speculate that most of the migration is due to the tidal disruption caused by merging satellites given the reduction in disc contribution to the spheroid once the merging activity is complete. We note that Debattista et al. (2004) showed that secular evolution accounted for some migration of stars from the disc to the spheroid in high-resolution simulations of isolated discs.

Satellites are expected to contribute a large mass of stars to the spheroid since stars are tidally stripped into spheroidal orbits. In the case of g15784's quiet merger history, the mass of the spheroid formed in satellites is similar to that formed in the inner 1 kpc and the disc. Finally, we note that the star formation in satellites is also largely confined to the unresolved central kpc similar to the main galaxy.

The large number of stars that form in the central kpc and disc echo the findings of Zolotov et al. (2009) and indicate that the predominant spheroid component is due in large part to stars that form in the main galaxy. However, satellites contribute a significant mass of stars to the spheroid and disrupt a large fraction of stars out of the disc, so these simulations do not exclude traditional spheroid creation through satellite mergers and tidal stripping.

4.5 Density profiles

From the simulations, one can find the three-dimensional distribution of all the matter in the galaxy as opposed to just that which is visible. Fig. 10 shows the resulting radial density profile. Particles are sorted by radius and placed into 1000 bins, each containing the same number of particles. The dark matter only profiles for every galaxy are shown as the grey solid lines. The dark matter and total density profiles are similar for each simulated galaxy. The dark matter profiles follow a r^{-3} power law or slightly shallower from the virial radius into $0.1r_{\mathrm{vir}}$ before growing shallower, similar to dark
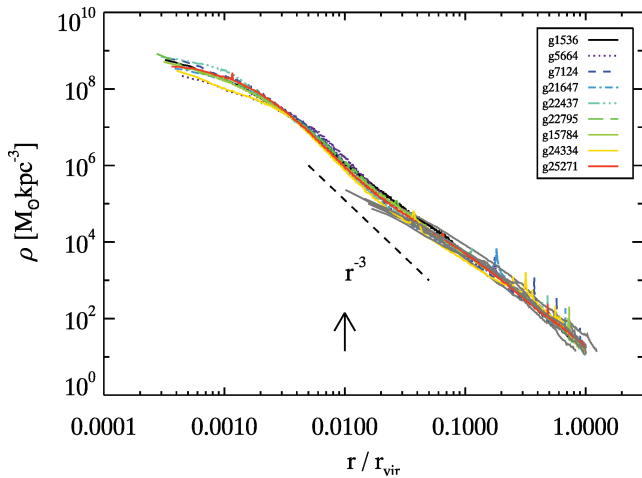
Figure 10. Particles are sorted by radius and placed into 1000 bins each containing the same number of particles. The radius of the bin is plotted as the mass-weighted mean of the particle radii for each bin. The total density profile (various colours) for each halo is compared with the profile of the dark matter from the simulations that include baryons (thin grey). The dark matter profile ends at a radius of $0.01r_{\rm vir}$, the radius inside which Power et al. (2003) determine the dark matter particles will take longer than the age of the Universe to relax.

matter only runs (Navarro, Frenk & White 1997; Moore et al. 1998; Reed et al. 2005). The total profile continues a steady rise along the power-law r^{-2} into 1 kpc (about $0.005r_{\rm vir}$) due to the stellar density before flattening out to a slope less than r^{-1} inside 1 kpc. Stars dominate the matter profile inside of 2 kpc.

4.6 Rotation curves

Rotation curves provide a comparison between the density profile found in these simulations and observations. Fig. 11 shows the circular velocity, $v_{\rm c}$ as a function of radius, where $v_{\rm c} = \sqrt{GM/R}$. Mock observations are not used because there is too much scatter in the star particle velocities at a given projected distance from the centre of the galaxy, so Fig. 11 is more properly called 'circular velocity curves', which might be exactly the same as the observed rotation curve.
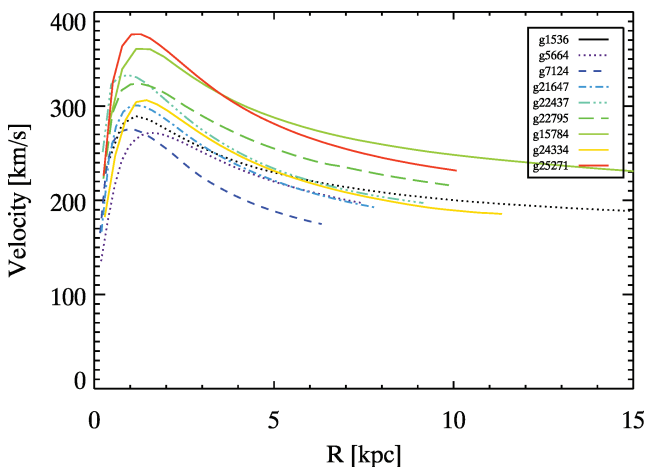

Figure 11. Circular velocity as a function of radius. The circular velocity (solid) defined as $v_{\rm c} = \sqrt{GM/r}$ in radial bins for each of our galaxies.
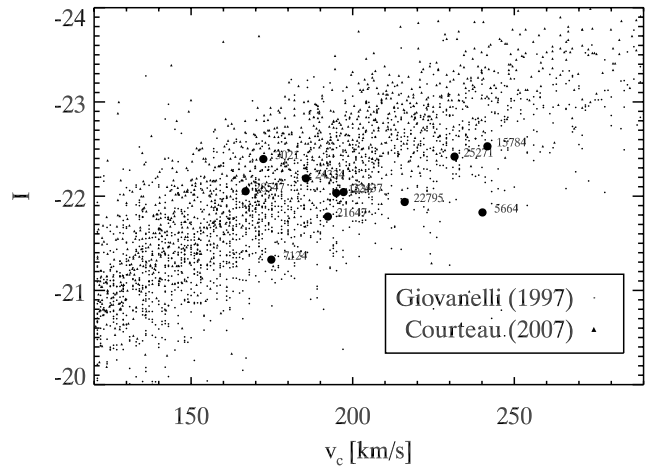

Figure 12. *I*-band absolute magnitude as a function of circular velocity at 3.5 disc scalelengths (*h*). The large dots represent the simulated galaxies while the small dots are from the Giovanelli et al. (1997) sample of cluster galaxies and the triangles are from Courteau et al. (2007).

The excessive bulge illustrated in Section 4.4 is again apparent in the rotation curves. Rather than exhibiting flat rotation curves as are observed, the simulated rotation curves all have a peak at the centre due to a large central concentration of mass. Governato et al. (2007) showed that increased resolution without any changes to star formation can also limit the central concentration of matter as the lessened impact of two-body interactions with halo dark matter particles minimizes angular momentum losses. Governato et al. (2010) show how higher resolution and consequent modifications to the star formation threshold density can limit the mass concentration in simulations of slightly less massive galaxies.

4.7 Tully–Fisher

The TF relationship shown in Fig. 12 compares the luminosity of a galaxy with its rotation velocity. Velocity indicates the dynamical mass for the inner parts of a galaxy, so the TF relationship indicates how bright a galaxy of a given mass should be. Most galaxies in the range of masses that we simulated have flat rotation curves, so the radius at which the rotation velocity is measured is irrelevant. In the simulations, however, the rotation curve rises sharply initially and then declines gradually with radius. We follow the example of Governato et al. (2007) and measure the rotation velocity at 3.5*h*. Governato et al. (2007) find in a resolution study that this is the radius at which velocity converges. It is unclear from Fig. 11 that the rotation curves are flat at this radius, but they are flatter than they are at smaller radii. The *I*-band magnitude for the galaxies generally matches the observations of the corresponding velocities, though the velocities remain slightly high. Governato et al. (2010) showed that higher resolution and higher star formation density threshold produce galaxies with more slowly rising rotation curves, so higher resolution simulations of these galaxies is an obvious next step.

4.8 Mass-to-light ratio

The relationship between the luminosity of a galaxy and the mass of its halo is a key observational question that provides constraints on semi-analytic models and strongly affects the interpretation of observational samples with respect to theoretical predictions about
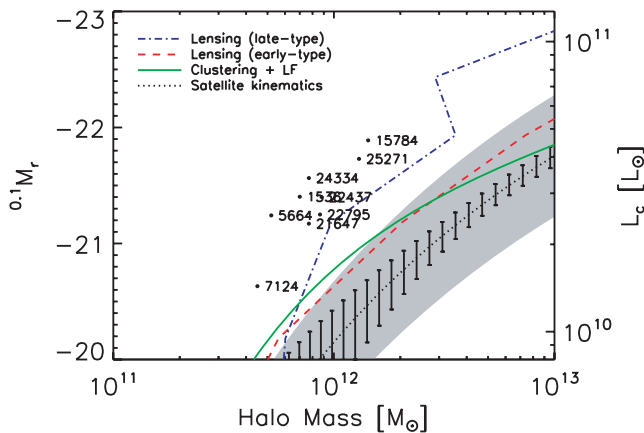
Figure 13. Galaxy luminosity in the $^{0.1}r$ band plotted as a function of the total halo mass including dark matter for the nine simulated MUGS galaxies. Observational measurements of the relationship between the halo mass and the luminosity of the central galaxy, L_c, are shown based on weak gravitational lensing (Mandelbaum et al. 2006), halo model fits to the galaxy clustering and luminosity function (Cacciato et al. 2009), and the kinematics of satellite galaxies (More et al. 2010, the 16th to 84th percentile confidence limit in the mean is shown by the error bars while the measured halo-to-halo dispersion is shown as the shaded region).

haloes. In Fig. 13, we have plotted the luminosity of our simulated galaxies versus their total (dark plus baryonic) mass. The luminosities are K-corrected to the $^{0.1}r$ band (the r band redshifted to $z = 0.1$) using KCORRECT v4.1.4 (Blanton et al. 2003) and the SUNRISE-generated SDSS gri magnitudes in order to facilitate making comparison to the observations.

By construction, our galaxies inhabit a relatively narrow band in halo mass, from $\sim 5 \times 10^{11}$ to $\sim 2 \times 10^{12}\, M_\odot$. Their luminosities cover a similar relative range in luminosity, from $\sim 1.5 \times 10^{10}$ to $\sim 5 \times 10^{10}\, L_\odot$, for a typical total mass-to-light ratio of ~ 30 within the virial radius.

We have overplotted a variety of observational estimates of the relationship between central galaxy luminosity and the total halo mass on to Fig. 13. These observational techniques are weak gravitational lensing (Mandelbaum et al. 2006, blue dot–dashed line for exponential-dominated late-type galaxies and red dashed line for de Vaucouleurs-dominated early-type galaxies), a halo model simultaneously fit to galaxy clustering and the luminosity function (Cacciato et al. 2009, solid green line), and the kinematics of satellite galaxies (More et al. 2010, dotted black line for the mean, error bars for the 16th to 84th percentile confidence limit of the mean and shaded grey region for the measured spread in central galaxy luminosity at a given halo mass). Note that while all of these studies are based on SDSS data, the techniques use completely independent properties of the galaxies to determine the halo mass. We have adopted $h = 0.73$, as used in the simulations, to convert the h-independent units used in these studies into physical units for direct comparison.

When comparing the observations to the simulations, it is important to realize that in the simulations, the systems are selected based on the halo mass, while the luminosity is an output of the simulations; we have therefore plotted the halo mass as the independent variable and the luminosity as the dependent variable in Fig. 13. However, in the observational studies, the galaxies are selected based on their luminosity and the halo mass is what is measured; therefore, the luminosity is the independent variable and the halo mass is the dependent variable. Cacciato et al. (2009) and More

et al. (2010) model the full relation between halo mass and central galaxy luminosity in order to determine $\langle \log L_c \rangle\,(M)$ rather than $\langle M \rangle\,(L_c)$, but are constrained at the low-mass end by the dearth of sufficiently faint galaxies in the observational sample, while Mandelbaum et al. (2006) explicitly measure $\langle M \rangle\,(L_c)$. This should be kept in mind when considering Fig. 13, and this is why the weak lensing result around late-type galaxies appears multivalued.

The halo mass–luminosity relationship for the simulated galaxies has the same shape and similar normalization as the observed relationship, particularly when comparing to the Mandelbaum et al. (2006) and Cacciato et al. (2009) results, or the blue subsample of More et al. (2010), which closely follows the Cacciato et al. results. The simulated galaxies are, however, all more luminous than the observed galaxies at a given halo mass, or equivalently the observed galaxies lie in more massive haloes at a given luminosity. This difference is no larger than the difference seen between observational techniques, so it may not be significant. One aspect of the simulated and observed samples that may be important is that the simulated galaxies are constrained not to lie near large group or cluster haloes; given the mass dependence of halo bias, those haloes are themselves likely to be more massive. However, it seems unlikely that this is the explanation given that the most isolated of the observational samples is that of More, van den Bosch & Cacciato (2009), with whom our results are the most discrepant. A more likely explanation is that this is another symptom of the overcooling problem, which turns too much of the gas in the system into stars and therefore results in an overluminous galaxy.

4.9 Star formation histories

One of the major ways to track the evolution of a galaxy is by examining when its stars formed. Fig. 14 shows the SFHs for each of our simulated galaxies. Peaks in the SFH correspond to merger events which drive starbursts. Mergers tidally disrupt disc gas and excite instabilities that cause gas overdensities (Mihos & Hernquist 1996; Springel 2000; Cox et al. 2006). Following the merger peaks, the shape of the SFH is an exponential increase followed by an exponential decline as the reservoir of gas is exhausted. The galaxies in Fig. 14 that have the most and latest mergers correspond to those with the least well-defined discs.
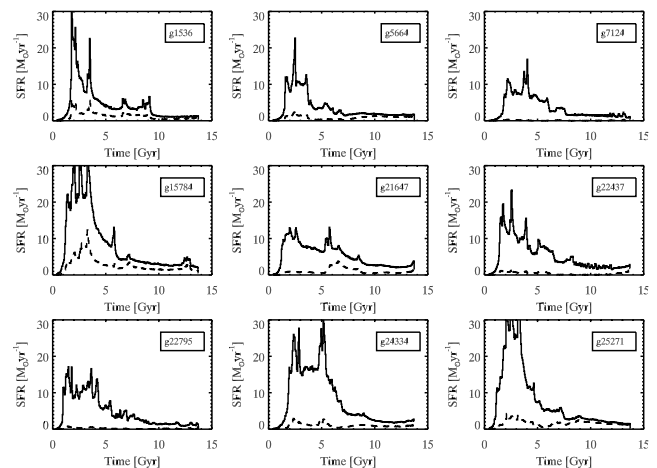

Figure 14. The star formation rate plotted as a function of time for all the stars inside $r_{\rm vir}$ (solid) and just stars that end up in the kinematically defined disc (dashed). Stars are sorted by their formation time into 50 Myr bins and the total mass of stars in that bin is divided by 50 Myr.
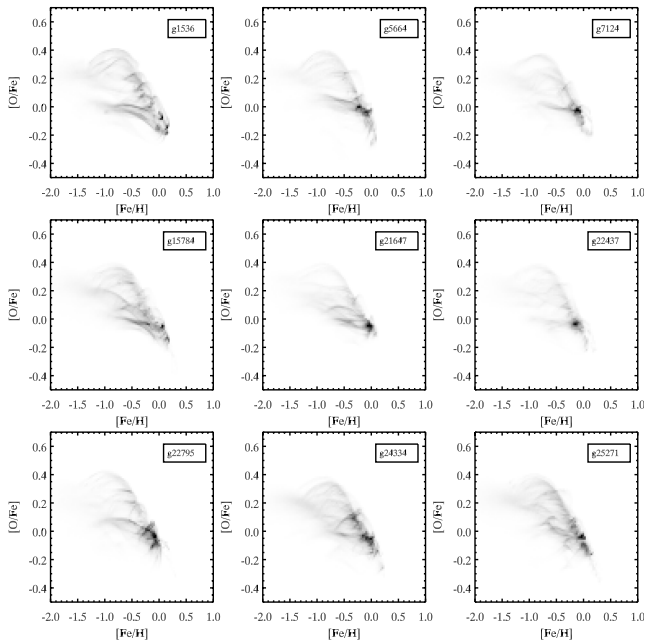
Figure 15. Metallicity distribution, [O/Fe] as a function of [Fe/H], of all the stars inside r_{vir} of the galaxy. Stars are sorted into 100×100 bins, 0.03 wide in [Fe/H] and 0.01 high in [O/Fe]. Evolution progresses from low [Fe/H] and high [O/Fe] to solar (0.0) [Fe/H] and [O/Fe]. The multiple evolutionary tracks through this diagram correspond to different stellar structures that each have their own SFH.

4.10 Metallicity evolution

Trends in metallicity help track the SFH of galaxies. Specifically, Fig. 15 shows the distribution of stars in [O/Fe] as a function of [Fe/H]. Evolution of metallicity proceeds from low [Fe/H] as stars form and produce iron that is ejected during SN explosions. SNe II occur on a shorter time-scale than SNeIa, and they eject alpha elements such as carbon, oxygen and silicon as well as iron. We use oxygen to track the abundance of alpha elements in our simulations. After stellar populations age for 40 Myr, SNeIa start to explode ejecting few alpha elements, but large quantities of iron. The range of [Fe/H] over which the [O/Fe] ratio remains high and constant indicates how many SNII explode before SNIa start contributing significant quantities of iron. Thus, regions of active star formation like the Milky Way disc will generate long, high [O/Fe] plateaus before [O/Fe] decreases due to the influx of iron from SNIa (Bensby et al. 2005; Reddy, Lambert & Allende Prieto 2006). Places where star formation is not as efficient like dwarf galaxies exhibit lower [O/Fe] at low [Fe/H] distinct from abundances of stars measured in the Milky Way's disc and halo (Venn et al. 2004). Models of galaxy formation that couple *N*-body simulations with analytic prescriptions for the stellar content of satellite galaxies are able to reproduce this dichotomy (Font et al. 2006).

Fig. 15 shows that the majority of the stars in the simulations form with solar metallicity and abundances. At low [Fe/H], stars form with both high and low [O/Fe]. The peak [O/Fe] values are 0.4, which are lower than the observed abundances of the disc, which have been observed up to 0.6 (Bensby et al. 2005; Reddy et al. 2006). This indicates a shortcoming of the simple power-law fit used for oxygen enrichment. The fit only allows SNeII from stars up to 40 M$_\odot$ to produce oxygen, so the chemical model does not capture chemical enrichment from more massive stars that produce more oxygen compared to iron (Woosley & Weaver 1995).

Much like observational galactic archaeology, the distinct metallicity evolution tracks apparent in Fig. 15 provide a useful alterative for discovering substructure inside galaxies as substructures exhibit stellar populations with different metallicity signatures. We leave further discussion of such methods for future work.

5 CONCLUSIONS

We presented nine galaxies from the MUGS simulated using *N*-body gravity and SPH. The galaxies are selected from a mass range around the mass of the Milky Way and from isolated environments, but their selection was otherwise unbiased for factors such as accretion history and angular momentum.

The galaxies were examined using the radiative transfer program SUNRISE to enable comparisons between the simulated galaxies and real galaxies in the observed plane. The simulated galaxies have colours and magnitudes that compare well with a sample of inclination corrected isolated galaxies from SDSS, and in particular separate into the well-known red sequence and blue cloud. However, both simulated populations tend too much towards the 'green valley', indicating that they contain more old stars than blue cloud galaxies and more young stars than galaxies along the red sequence.

The surface brightness profiles of nearly all the simulated galaxies can be fit with exponential discs combined with a central de Vaucouleurs $r^{1/4}$ law similar to real galaxies. However, the proportion of B/T ratios is higher than what is typically observed. The B/T ratios are also high when the stars are decomposed into the spheroid and disc based on their kinematics. There are no galaxies with a B/T ratios less than 0.5 whereas observed samples find many galaxies with B/T < 0.5. This result is similar to that found in many previous simulations. We note that many of the recently formed stars that are classified as part of the spheroid form with orbits in the disc plane in the central regions of the disc. We also note that most of the stars that comprise the spheroid formed in situ, but we leave the question of how the stars may migrate from the disc to a spherical distribution for future work.

As to the question of why galaxies form with more or less spheroid, there seems to be a modest trend with accretion history. We find that the largest discs (g1536 and g15784) form with a quiet merger history in which they had their last major merger prior to $z = 3$, while the largest bulges all resulted from recent last major mergers. There also appears to be a dependence on halo spin as g25271 has a relatively quiet merger history, but low λ' and results in a significant bulge and red colour. Since all the galaxies used in MUGS fall in a limited mass range, these conclusions do not include the impact of mass.

We compare the brightness of the final galaxies with their mass at two different radii in the final output. First, we compare our galaxies with the observed TF relationship that probes the amount of light a galaxy produces with the mass contained in its inner regions. Since the final mass concentration of all the galaxies is too high, we use a rotation velocity from 3.5 disc scalelengths away from the galaxy centre. Previous studies have shown that this is the radius at which rotation velocities converge. The galaxies are still slightly *fainter* than the observed sample based on these inner velocities. Secondly, we compare the brightness of our galaxies with observations of the whole halo mass derived using a number of different methods. In each case, the simulated galaxies are *brighter* than comparable observed galaxies at the same mass. This indicates that too many stars form in the simulation. The high central velocities used in the TF relationship indicate that mass gets too concentrated at the centres of the haloes and while the galaxies are fainter than the

observed TF relationship, the lack of resolution makes it difficult to determine whether the amount of stars formed is too many or too few.

We are thus left with the challenge of creating more realistic simulations in order to obtain more accurate insights into how the important physical processes involved in galaxy formation result in the observed population of galaxies. Fortunately, there has been much recent work that guides the way forward. It has been shown repeatedly that higher resolution makes better discs (Governato et al. 2004, 2007). More recently, it has been shown that high resolution combined with clustered star formation can remove central density concentrations from dwarf galaxies (Mashchenko, Wadsley & Couchman 2008; Governato et al. 2010).

While these simulations open many possibilities for expanding our understanding of how galaxies form, they also show that there is much work left to be done before we can claim to have simulated a sample of galaxies that compares well with real ones.

ACKNOWLEDGMENTS

REFERENCES

Abadi M. G., Navarro J. F., Steinmetz M., 2006, MNRAS, 365, 747
Abel T., Anninos P., Zhang Y., Norman M. L., 1997, New Astron., 2, 181
Allen P. D., Driver S. P., Graham A. W., Cameron E., Liske J., de Propris R., 2006, MNRAS, 371, 2
Bailin J., Harris W. E., 2008, ApJ, 681, 225
Barnes J., Hut P., 1986, Nat, 324, 446
Barnes J. E., Hernquist L., 1996, ApJ, 471, 115
Belokurov V. et al., 2006, ApJ, 642, L137
Bensby T., Feltzing S., Lundström I., Ilyin I., 2005, A&A, 433, 185
Benson A. J., Devereux N., 2010, MNRAS, 402, 2321
Benson A. J., Bower R. G., Frenk C. S., Lacey C. G., Baugh C. M., Cole S., 2003, ApJ, 599, 38
Binney J., Merrifield M., 1998, Galactic astronomy. Princeton Univ. Press, Princeton
Black J. H., 1981, MNRAS, 197, 553
Blanton M. R. et al., 2003, AJ, 125, 2348
Brook C. B., Kawata D., Martel H., Gibson B. K., Bailin J., 2006, ApJ, 639, 126
Brooks A. M., Governato F., Booth C. M., Willman B., Gardner J. P., Wadsley J., Stinson G., Quinn T., 2007, ApJ, 655, L17
Brooks A. M., Governato F., Quinn T., Brook C. B., Wadsley J., 2009, ApJ, 694, 396
Bullock J. S., Johnston K. V., 2005, ApJ, 635, 931
Bullock J. S., Dekel A., Kolatt T. S., Kravtsov A. V., Klypin A. A., Porciani C., Primack J. R., 2001, ApJ, 555, 240

Cacciato M., van den Bosch F. C., More S., Li R., Mo H. J., Yang X., 2009, MNRAS, 394, 929
Cen R., 1992, ApJS, 78, 341
Ceverino D., Klypin A., 2009, ApJ, 695, 292
Cole S., Lacey C. G., Baugh C. M., Frenk C. S., 2000, MNRAS, 319, 168
Colless O. et al., 2001, MNRAS, 328, 1039
Courteau S., Dutton A. A., van den Bosch F. C., MacArthur L. A., Dekel A., McIntosh D. H., Dale D. A., 2007, ApJ, 671, 203
Cox D. P., 2005, ARA&A, 43, 337
Cox T. J., Jonsson P., Primack J. R., Somerville R. S., 2006, MNRAS, 373, 1013
Dalcanton J. J., Spergel D. N., Summers F. J., 1997, ApJ, 482, 659
Davis M., Efstathiou G., Frenk C. S., White S. D. M., 1985, ApJ, 292, 371
Debattista V. P., Carollo C. M., Mayer L., Moore B., 2004, ApJ, 604, L93
D'Onghia E., Navarro J. F., 2007, MNRAS, 380, L58
Dutton A. A., 2009, MNRAS, 396, 121
Eggen O. J., Lynden-Bell D., Sandage A. R., 1962, ApJ, 136, 748
Fall S. M., Efstathiou G., 1980, MNRAS, 193, 189
Ferland G. J., Korista K. T., Verner D. A., Ferguson J. W., Kingdon J. B., Verner E. M., 1998, PASP, 110, 761
Font A. S., Johnston K. V., Bullock J. S., Robertson B. E., 2006, ApJ, 638, 585
Gerritsen J. P. E., 1997, PhD thesis, Univ. Gronigen
Giovanelli R., Haynes M. P., Herter T., Vogt N. P., da Costa L. N., Freudling W., Salzer J. J., Wegner G., 1997, AJ, 113, 53
Governato F. et al., 2004, ApJ, 607, 688
Governato F., Willman B., Mayer L., Brooks A., Stinson G., Valenzuela O., Wadsley J., Quinn T., 2007, MNRAS, 374, 1479
Governato F. et al., 2009, MNRAS, 398, 312
Governato F. et al., 2010, Nat, 463, 203
Haardt F., Madau P., 1996, ApJ, 461, 20
Harris W. E., 1996, AJ, 112, 1487
Jonsson P., 2006, MNRAS, 372, 2
Kazantzidis S., Bullock J. S., Zentner A. R., Kravtsov A. V., Moustakas L. A., 2008, ApJ, 688, 254
Kennicutt R. C., 1998, ApJ, 498, 541
Kereš D., Katz N., Weinberg D. H., Davé R., 2005, MNRAS, 363, 2
Knollmann S. R., Knebe A., 2009, ApJS, 182, 608
Kormendy J., 1993, in Dejonghe H., Habing H. J., eds, Proc. IAU Symp. 153, Galactic Bulges. Kluwer, Dordrecht, p. 209
Kroupa P., Tout C. A., Gilmore G., 1993, MNRAS, 262, 545
Lada C. J., Lada E. A., 2003, ARA&A, 41, 57
Leitherer C. et al., 1999, ApJS, 123, 3
Lelli F., Fraternali F., Sancisi R., 2010, A&A, 516, 11
Lupton R., Blanton M. R., Fekete G., Hogg D. W., O'Mullane W., Szalay A., Wherry N., 2004, PASP, 116, 133
Majewski S. R., 1993, ARA&A, 31, 575
Mandelbaum R., Seljak U., Kauffmann G., Hirata C. M., Brinkmann J., 2006, MNRAS, 368, 715
Martínez-Serrano F. J., Serna A., Doménech-Moral M., Domínguez-Tenreiro R., 2009, ApJ, 705, L133
Mashchenko S., Wadsley J., Couchman H. M. P., 2008, Sci, 319, 174
McCray R., Kafatos M., 1987, ApJ, 317, 190
McKee C. F., Ostriker J. P., 1977, ApJ, 218, 148
Mihos J. C., Hernquist L., 1996, ApJ, 464, 641
Mo H. J., Mao S., White S. D. M., 1998, MNRAS, 295, 319
Moore B., Governato F., Quinn T., Stadel J., Lake G., 1998, ApJ, 499, L5
More S., van den Bosch F. C., Cacciato M., 2009, MNRAS, 392, 917
More S., van den Bosch F. C., Cacciato M., Skibba R., Mo H. J., Yang X., 2010, MNRAS, submitted (arXiv:1003.3203)
Navarro J. F., Benz W., 1991, ApJ, 380, 320
Navarro J. F., Steinmetz M., 2000, ApJ, 538, 477
Navarro J. F., Frenk C. S., White S. D. M., 1997, ApJ, 490, 493
Okamoto T., Frenk C. S., 2009, MNRAS, 399, L174
Okamoto T., Eke V. R., Frenk C. S., Jenkins A., 2005, MNRAS, 363, 1299
Oppenheimer B. D., Davé R., 2006, MNRAS, 373, 1265
Pearce F. R. et al., 1999, ApJ, 521, L99

Piontek F., Steinmetz M., 2009, MNRAS, submitted (arXiv:0909.4167)

Piskunov A. E., Kharchenko N. V., Schilbach E., Röser S., Scholz R., Zinnecker H., 2008, A&A, 487, 557

Power C., Navarro J. F., Jenkins A., Frenk C. S., White S. D. M., Springel V., Stadel J., Quinn T., 2003, MNRAS, 338, 14

Quinn P. J., Hernquist L., Fullagar D. P., 1993, ApJ, 403, 74

Quinn T., Binney J., 1992, MNRAS, 255, 729

Raiteri C. M., Villata M., Navarro J. F., 1996, A&A, 315, 105

Reddy B. E., Lambert D. L., Allende Prieto C., 2006, MNRAS, 367, 1329

Reed D., Governato F., Verde L., Gardner J., Quinn T., Stadel J., Merritt D., Lake G., 2005, MNRAS, 357, 82

Robertson B., Yoshida N., Springel V., Hernquist L., 2004, ApJ, 606, 32

Ryden B. S., 1988, ApJ, 329, 589

Sánchez-Blázquez P., Courty S., Gibson B. K., Brook C. B., 2009, MNRAS, 398, 591

Scannapieco C., Tissera P. B., White S. D. M., Springel V., 2008, MNRAS, 389, 1137

Scannapieco C., White S. D. M., Springel V., Tissera P. B., 2009, MNRAS, 396, 696

Schaye J. et al., 2010, MNRAS, 402, 1536

Searle L., Zinn R., 1978, ApJ, 225, 357

Seljak U., Zaldarriaga M., 1996, ApJ, 469, 437

Somerville R. S., Hopkins P. F., Cox T. J., Robertson B. E., Hernquist L., 2008, MNRAS, 391, 481

Spergel D. N. et al., 2007, ApJS, 170, 377

Springel V., 2000, MNRAS, 312, 859

Springel V., Hernquist L., 2003a, MNRAS, 339, 289

Springel V., Hernquist L., 2003b, MNRAS, 339, 312

Springel V., Hernquist L., 2005, ApJ, 622, L9

Stinson G., Seth A., Katz N., Wadsley J., Governato F., Quinn T., 2006, MNRAS, 373, 1074

Thacker R. J., Couchman H. M. P., 2000, ApJ, 545, 728

Thielemann F.-K., Nomoto K., Yokoi K., 1986, A&A, 158, 17

Toth G., Ostriker J. P., 1992, ApJ, 389, 5

van den Bosch F. C., 2001, MNRAS, 327, 1334

Velazquez H., White S. D. M., 1999, MNRAS, 304, 254

Venn K. A., Irwin M., Shetrone M. D., Tout C. A., Hill V., Tolstoy E., 2004, AJ, 128, 1177

Verner D. A., Ferland G. J., 1996, ApJS, 103, 467

Wadsley J. W., Stadel J., Quinn T., 2004, New Astron., 9, 137

Woosley S. E., Weaver T. A., 1995, ApJS, 101, 181

Yang X., Mo H. J., van den Bosch F. C., Pasquali A., Li C., Barden M., 2007, ApJ, 671, 153

York A. et al., 2000, AJ, 120, 1579

Zolotov A., Willman B., Brooks A. M., Governato F., Brook C. B., Hogg D. W., Quinn T., Stinson G., 2009, ApJ, 702, 1058

This paper has been typeset from a TeX/LaTeX file prepared by the author.